

# DESY SUMMER STUDENT PROJECT



**Bc. Vladimír Vojtek**

*(DESY summer student 2013)*

*Date of birth:*

August 20, 1989

*Nationality:*

Slovak

## **Study of disordered materials by pair distribution function**

*Area of research:*

Photon Physics, Material Science

*Time frame:*

July 16 – September 5, 2013



*Supervisor:*

Dr. Jozef Bednarcík

Deutsches Elektronen Synchrotron DESY

Notkestr. 85

22607 Hamburg, Germany

email: [jozef.bednarcik@desy.de](mailto:jozef.bednarcik@desy.de)

phone: +49-40-89981861

## Short description of the research project

This projects dealt with methodology of calculation of the atomic pair distribution function from data obtained by two-dimensional detector. Individual data corrections and calculation steps are described in detail. Analysis of in-situ XRD data in real space by pair distribution function was demonstrated by investigation of volume thermal expansion of amorphous  $\text{Fe}_{76}\text{Mo}_8\text{Cu}_1\text{B}_{15}$  alloy. Obtained results show that non-magnetic technique such as XRD allows observation of ferromagnetic-to-paramagnetic transition of metallic glass, which was determined as a change of the slope of its expansion curve.



## Contents

<b>1</b>	<b>Introduction</b>	<b>1</b>
<b>2</b>	<b>Goals of the research project</b>	<b>1</b>
<b>3</b>	<b>Experimental part</b>	<b>2</b>
3.1	Preparation of samples . . . . .	2
3.2	High-energy X-ray diffraction at P02.1 . . . . .	2
<b>4</b>	<b>Calculation of Structure factor</b>	<b>3</b>
4.1	Data corrections . . . . .	3
4.1.1	Parasitic scattering correction . . . . .	5
4.1.2	Absorption correction . . . . .	5
4.1.3	Normalization . . . . .	7
4.1.4	Compton scattering correction . . . . .	7
4.1.5	Laue diffuse correction (atomic scattering factors) . . . . .	8
<b>5</b>	<b>Pair distribution function</b>	<b>9</b>
<b>6</b>	<b>In situ X-ray diffraction</b>	<b>10</b>
<b>7</b>	<b>Conclusions</b>	<b>13</b>
	<b>Acknowledgement</b>	<b>13</b>
	<b>References</b>	<b>13</b>

## 1 Introduction

The pair distribution function (PDF) represents variations of atomic density  $\rho(r)$  with respect to the mean atomic density  $\rho_0$ . In other words the PDF is a measure of the probability of finding an atom at a distance  $r$  from another atom and gives information about both average and the local structure of materials (see Figure 1). The pair distribution function (PDF) is widely used to obtain detailed knowledge of the atomic-scale structure [1, 2].

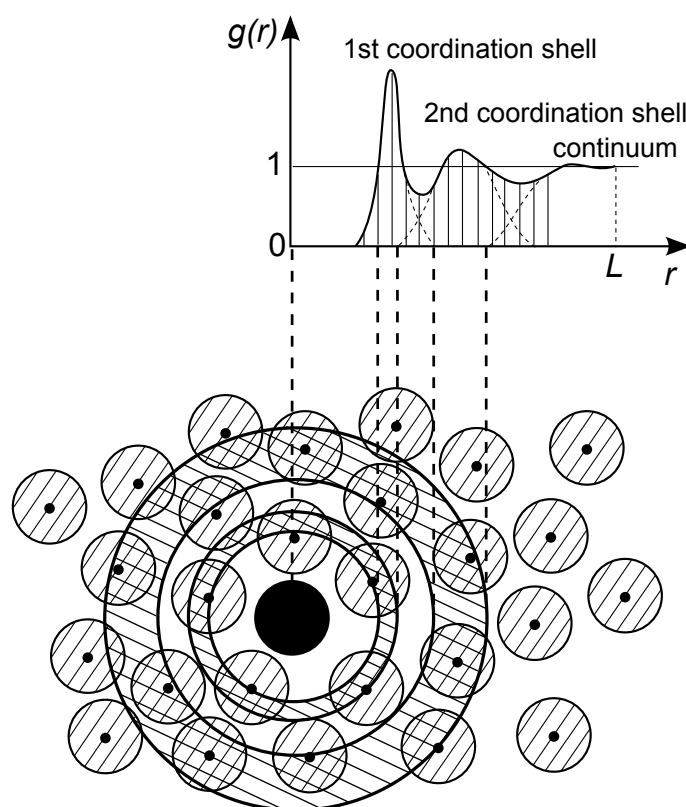


**Figure 1:** The atomic pair distribution function for amorphous material [3].

## 2 Goals of the research project

The main goal of this project is study of disordered materials by the pair distribution function. Goals of this project can be divided in to two main parts:

- methodology of data-collection with an area (2D) detector and calculation of the atomic pair distribution function (PDF),
- demonstration of PDF method on real datasets obtained from XRD measurement.

### 3 Experimental part

#### 3.1 Preparation of samples

Amorphous alloys with nominal composition  $\text{Pd}_{81}\text{Si}_{19}$  and  $\text{Fe}_{76}\text{Mo}_8\text{Cu}_1\text{B}_{15}$  in the form of thin ribbons ( $40\text{ }\mu\text{m}$ ) were prepared by single roller melt spinning technique.

#### 3.2 High-energy X-ray diffraction at P02.1

X-ray diffraction experiments (XRD) were performed in transmission geometry at the P02.1 beamline, which operates at the fixed photon energy of 60 keV ( $\lambda = 0.20727\text{ }\text{\AA}$ ). Experimental setup used for this type of measurements is schematically drawn in Figure 2.

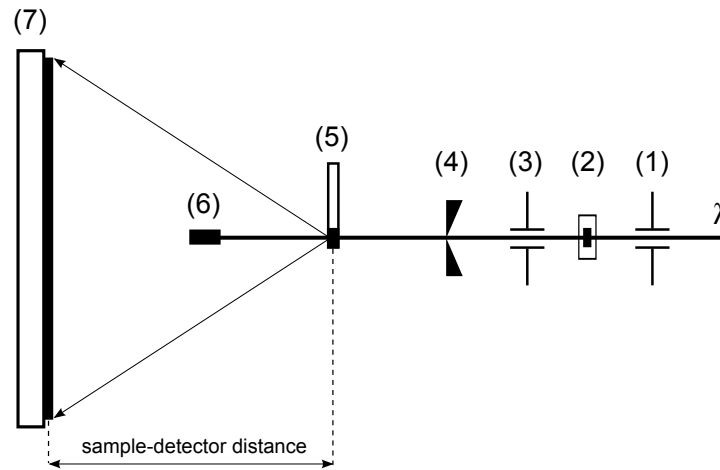


**Figure 2:** Schematic drawing of the experimental setup at P02.1 beamline used for X-ray diffraction measurements: (1) primary slits, (2) small shutter, (3) secondary slits, (4) pin hole, (5) sample in capillary, (6) beam stop, (7) detector Perkin Elmer 1621

The direct X-ray beam, whose profile is defined by primary slits ( $0.7 \times 0.7\text{ mm}^2$ ), traverses through the small shutter, which defines exposure (illumination) time. Behind the shutter, there are situated the secondary slits, which define the profile of the direct beam (cross section:  $1 \times 1\text{ mm}^2$ ) and remove any air scattering and parasitic scattering originating from the primary slits. The pin hole, placed closely in front of the sample, also helps to suppress any parasitic air scattering, which may occur during beam transport. The beam stop, whose role is to stop the direct X-ray beam (thereby it protects the detector), is installed nearly behind the sample and thus eliminates additional air scattering of direct beam. The last important part of used experimental setup is the 2D detector, which collects diffracted photons diffracted by the sample.

XRD experiments for this project were acquired at room temperature and fast image plate detector Perkin Elmer 1621 ( $2048 \times 2048$  pixels,  $200 \times 200\text{ }\mu\text{m}^2$  pixel size) carefully mounted orthogonal to the X-ray beam was used. The distance between 2D detector

and sample was adjusted to 19.3 cm in order to cover high- $q$  range ( $q = 4\pi\sin(\theta)/\lambda$ , where  $2\theta$  is the scattering angle) up to  $19 \text{ \AA}^{-1}$ .  $\text{CeO}_2$  standard was used to calibrate the sample-to-detector distance and tilt of the imaging plate relative to the beam path. About 5 independent scans were averaged to attain optimum counting statistics. Each measurement was followed by background scan, which was later removed from the sample scan.

The result of X-ray diffraction measurement with using of 2D detector is a diffraction pattern shown in Figure 3, but for next data analysis, it is better to interpret this pattern in form of radially averaged pattern. For this reason, the two-dimensional XRD patterns were integrated to the  $q$ -space using the software package FIT2D (Figure 4).

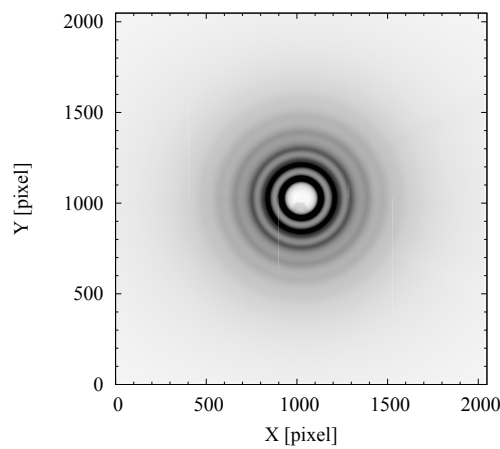


**Figure 3:** Diffuse diffraction pattern of fully amorphous  $\text{Pd}_{81}\text{Si}_{19}$  ribbon.

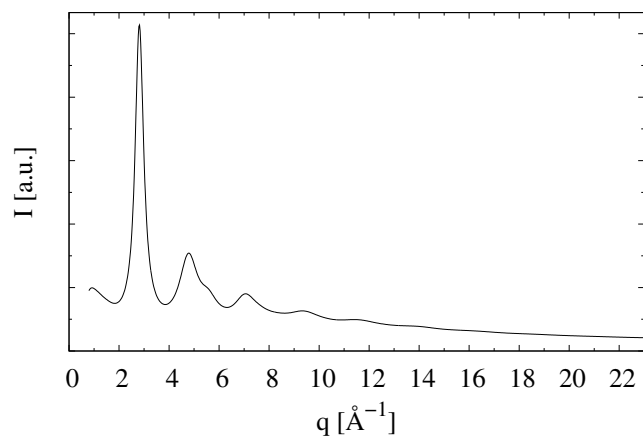


**Figure 4:** Radially averaged XRD pattern, obtained by integrating of 2D XRD patterns for amorphous  $\text{Pd}_{81}\text{Si}_{19}$  sample.

## 4 Calculation of Structure factor

### 4.1 Data corrections

The measured X-ray diffraction intensity may be expressed by [4]

$$I^{mea}(q) = PA[N(I_{eu}^{coh} + I_{eu}^{inc} + I_{eu}^{mul})] \quad (1)$$

where  $P$  is polarization factor,  $A$  the absorption factor,  $N$  the normalization constant, and  $I_{eu}^{coh}$ ,  $I_{eu}^{inc}$ ,  $I_{eu}^{mul}$  are the coherent, incoherent (Compton), and multiple scattering intensities, respectively, in electron units. According Faber-Ziman formalism [5] the structure function,  $(S(q))$ , can be defined in the following form

$$S(q) = \frac{I_{eu}^{coh}(q) - \left\{ \left[ \sum_{i=1}^n c_i f_i^2(q) \right] - \left[ \sum_{i=1}^n c_i f_i(q) \right]^2 \right\}}{\left[ \sum_{i=1}^n c_i f_i(q) \right]^2} \quad (2)$$

where  $c_i$  and  $f_i(q)$  are the atomic concentration and scattering factor of the atomic species of type  $i$  ( $i = \text{Pd, Si}$ ), respectively. Depending on concentration and X-ray scattering power of specific element, each atomic partial contributes with different weight  $w_{ij}$  to the total structure factor  $S(q)$

$$S(q) = \sum_{ij} w_{ij}(q) S_{ij}(q) \quad (3)$$

In case of X-ray diffraction weighting factors  $w_{ij}$  depend on  $q$  and can be calculated using equation

$$w_{ij}(q) = \frac{(2 - \delta_{ij})c_i c_j f_i(q) f_j(q)}{\left[ \sum_{k=1}^n c_k f_k(q) \right]^2} \quad (4)$$

where  $\delta_{ij}$  is Kronecker delta function ( $\delta_{ij}=1$  for  $i=j$  and  $\delta_{ij}=0$  for  $i \neq j$ ),  $c$  and  $f(q)$  are concentration and scattering factor of atomic species of type  $i, j$  ( $i, j = \text{Pd, Si}$ ), respectively.

Calculated  $q$ -dependance of structure factor for investigated  $\text{Pd}_{81}\text{Si}_{19}$  sample is shown in Figure 5. Figure 6 shows  $q$ -dependence of X-ray weighting factors calculated according equation 4 for individual atomic pairs.

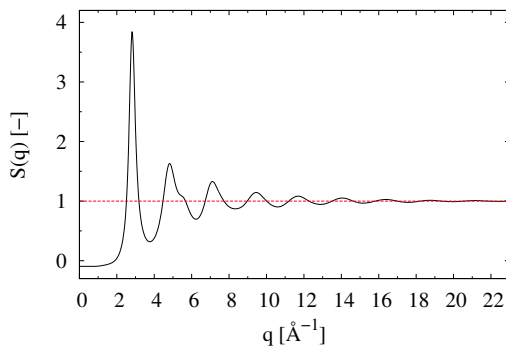


**Figure 5:** X-ray total structure factor  $S(q)$  for  $\text{Pd}_{81}\text{Si}_{19}$  alloy.

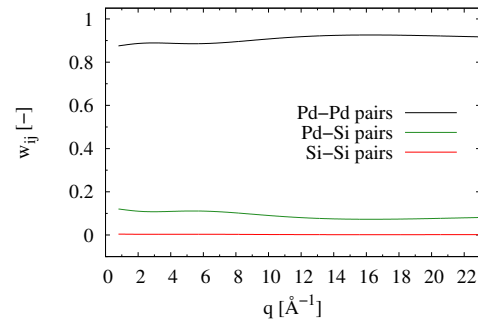


**Figure 6:**  $q$ -dependence of X-ray weighting factors calculated according equation 4 for Pd-Pd, Pd-Si and Si-Si pairs.

In order to recover coherently scattered intensity  $I_{eu}^{coh}$  from the measured one  $I^{mea}$ , one has to usually perform series of corrections, which are listed below:

1. Parasitic (air, sample container) scattering correction
2. Multiple scattering correction
3. Polarization correction
4. Absorption correction
5. Normalization

## 6. Inelastic (Compton) scattering correction

## 7. Laue diffuse correction

Individual data corrections for binary  $\text{Pd}_{81}\text{Si}_{19}$  alloy in the form of thin ribbon are demonstrated in the following subsections. Due to its very small thickness (around  $40\text{ }\mu\text{m}$ ) and relatively low absorption, multiple scattering can be neglected. Since diffracted photons were collected with two-dimensional detector (PE 1621) and complete Debye-Scherrer rings were radially integrated polarization correction effectively cancels out.

### 4.1.1 Parasitic scattering correction

Data acquired by the area detector contain not only signal from the sample, but also parasitic signal from air and sample container scattering which has to be subtracted from measured data. For this reason, it is always necessary to acquire diffraction pattern only of sample container and also one pattern without any sample or container, but with exactly the same setup parameters as for the sample. Investigated  $\text{Pd}_{81}\text{Si}_{19}$  sample was standing free (without any container) during measurement, so in this case it was necessary to acquire diffraction pattern only of air scattering and this signal was deducted from data of measurement with the sample (Figure 7).

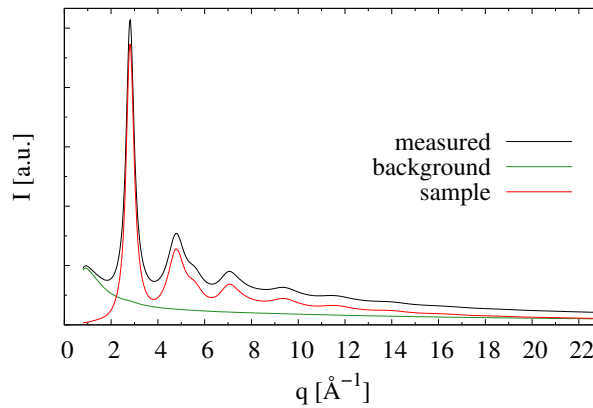


**Figure 7:** Measured XRD pattern of the sample with background, of background and calculated pattern only of the  $\text{Pd}_{81}\text{Si}_{19}$  sample.

### 4.1.2 Absorption correction

Absorption process is the process in which the intensity of photon beam is decreasing during it travels through the matter. Quantitatively, the absorption is given by the linear absorption coefficient  $\mu_s$ . By definition  $\mu_s dx$  is the attenuation of the beam through an

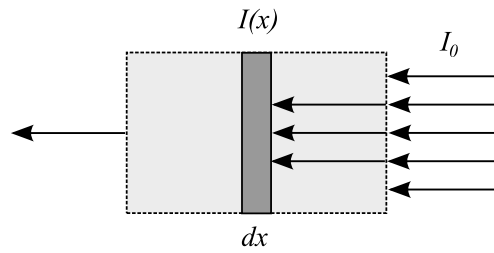


**Figure 8:** The attenuation of an X-ray beam through a sample due to absorption.

infinitesimal sheet of thickness  $dx$  at a depth  $x$  from the surface (Figure 8). The intensity  $I(x)$  through the sample must therefore fulfill the condition

$$-dI = I(x)\mu_s dx \quad (5)$$

which leads to the differential equation

$$\frac{dI}{I(x)} = -\mu_s dx \quad (6)$$

The solution is found by requiring that  $I(x = 0) = I_0$ , the incident beam intensity at  $x = 0$ , and we have

$$I = I_0 \exp(-\mu_s x) \quad (7)$$

Absorption coefficient can be also expressed in form of the absorption length  $\delta_s$ , where  $\delta_s = 1/\mu_s$  and it corresponds the length at which the intensity of photon beam decreases by factor  $1/e$  [6].

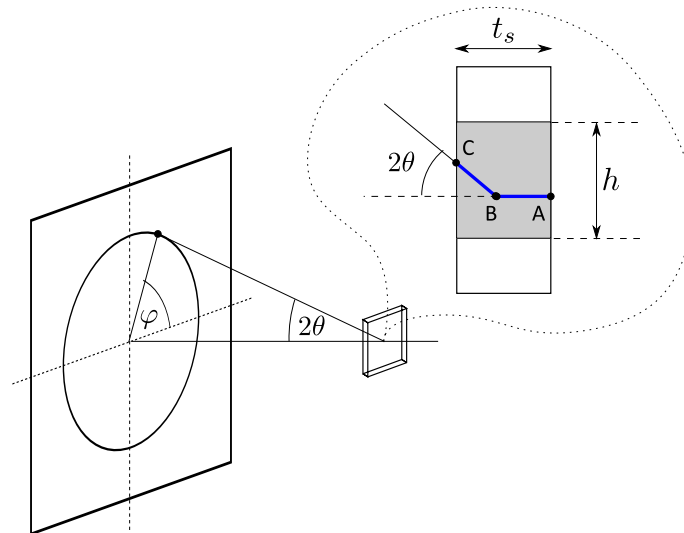


**Figure 9:** Schematic sketch showing arrangement of plate shaped sample measured in transmission geometry with 2D detector. The inset shows side view of the sample illuminated by beam with height  $h$ .

Figure 9 shows the typical arrangement of components during XRD transmission experiment, in which the sample is in the form of thin sheet, incoming photon beam



is perpendicular to its surface and data are collected by 2D detector. Due to symmetry reasons, diffracted photons leaving sample at angle  $2\theta$  travel the same path through the sample and thus show no dependence on azimuth angle  $\varphi$ . In this case, one can derive expression for absorbed  $2\theta$  dependence of transmitted intensity [7]

$$I(2\theta) = I_0 \exp(-\mu_s t_s) \frac{\exp[\mu_s t_s (1 - \sec 2\theta)] - 1}{\mu_s t_s (1 - \sec 2\theta)}, \quad (8)$$

where  $\sec(2\theta) = 1/\cos(2\theta)$  and absorption factor in eq. 1 on page 3 is equal to  $A = I_0/I(2\theta)$ .

#### 4.1.3 Normalization

The measured X-ray intensity is arbitrary value. The intensity should be normalized properly to get physical meaning. To determine normalization constant,  $N$ , high  $q$  part of data was used. In this method, the normalization constant,  $N$  is defined in the following way

$$N = \frac{\int_{q_{mid}}^{q_{max}} \left[ \sum_{i=1}^n c_i f_i^2(q) \right] + I_{eu}^{inc}(q) \, dq}{\int_{q_{mid}}^{q_{max}} [I^{cor}(q)] \, dq} \quad (9)$$

where  $I^{cor}$  corresponds to the data after corrections for background, multiple scattering, polarization, and absorption,  $q_{mid} \approx 50 - 60 \% q_{max}$ .

#### 4.1.4 Compton scattering correction

According work of Thijsee [8] the Compton profile was calculated using following equation

$$I_{eu}^{inc}(q) = R \sum_{j=1}^n c_j Z_j \frac{(b_j q)^{a_j}}{1 + (b_j q)^{a_j}} \quad (10)$$

where  $Z$  correspond to atomic number and  $R$  is defined as

$$R = \left( \frac{\lambda}{\lambda'} \right)^p = \frac{1}{\left( 1 + \frac{2h}{mc} \frac{\sin^2 \theta}{\lambda} \right)^p} \quad (11)$$

and coefficients  $a_j$  and  $b_j$  can be expressed as

$$a_j = 2.6917 Z_j^{-1} + 1.2450 \quad (12)$$

$$b_j = 1.1870 Z_j^{-1} + 0.1075 + 0.00436 Z_j - (0.01543 Z_j)^2 + (0.01422 Z_j)^3. \quad (13)$$

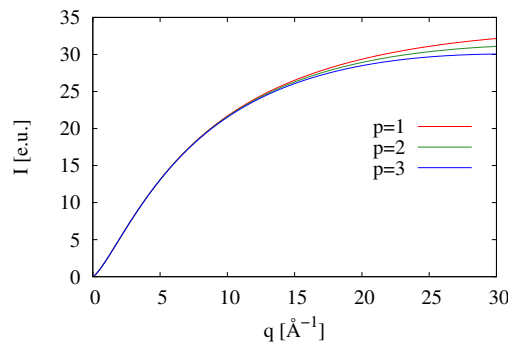


**Figure 10:** Compton profiles calculated using eq. 10 with various values of exponent  $p$  for binary alloy  $\text{Pd}_{81}\text{Si}_{19}$ .

Figure 10 shows Compton profiles calculated using eq. 10 with various values of exponent  $p$  for binary alloy  $\text{Pd}_{81}\text{Si}_{19}$ .

#### 4.1.5 Laue diffuse correction (atomic scattering factors)

Atomic scattering factor (ASF) depends on atomic number and scattering angle,  $\theta$ . According work of Waasmaier and Kirfel [9] ASF can be approximated by following formula

$$f(q) = c + \sum_{i=1}^n a_i \exp\left(-b_i \left[\frac{q}{4\pi}\right]^2\right), \quad q = \frac{4\pi \sin \theta}{\lambda}. \quad (14)$$

As can be seen in Figure 11, ASF increases with increasing atomic number and rapidly decreases with increasing scattering angle. Figure 12 shows composition weighted ASF and Laue diffuse term for binary  $\text{Pd}_{81}\text{Si}_{19}$  alloy, where  $\langle f^2 \rangle = [\sum_{i=1}^n c_i f_i^2(q)]$  and  $\langle f \rangle^2 = [\sum_{i=1}^n c_i f_i(q)]^2$ .

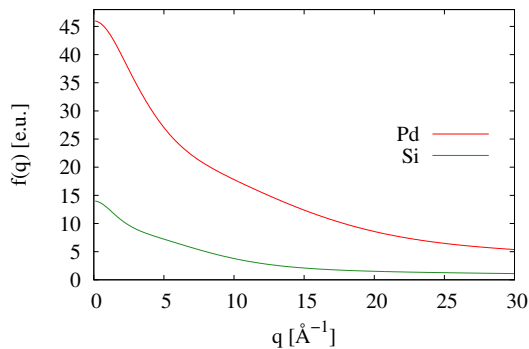


**Figure 11:** Atomic scattering factors for Pd and Si atoms.

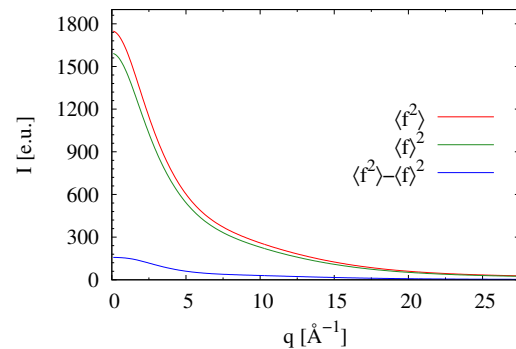


**Figure 12:** Composition weighted ASF and Laue diffuse term for binary  $\text{Pd}_{81}\text{Si}_{19}$  alloy.

## 5 Pair distribution function

The total reduced pair distribution function,  $G(r)$ , can be obtained through a sine Fourier transform of the total-scattering structure function  $S(q)$

$$G(r) = 4\pi r[\rho(r) - \rho_0] = \frac{2}{\pi} \int_0^{q_{max}} q[S(q) - 1]\sin(rq) dq \quad (15)$$

where  $\rho$  and  $\rho_0$  are the *local* and *average* atomic number densities, respectively,  $r$  is the radial distance, and  $q$  is the magnitude of the scattering vector [4, 10, 11]. From  $G(r)$  the pair distribution function,  $g(r)$ , and radial distribution function,  $RDF(r)$ , can be calculated by

$$g(r) = \frac{\rho(r)}{\rho_0} = \frac{G(r)}{4\pi\rho_0 r} + 1 \quad (16)$$

$$RDF(r) = 4\pi r^2 \rho(r) = 4\pi\rho_0 r^2 + rG(r) \quad (17)$$

The average coordination number,  $CN$ , around any given atom in a spherical shell between radius  $r_1$  and  $r_2$  can be calculated as

$$CN = \int_{r_1}^{r_2} RDF(r) dr. \quad (18)$$

The PDF defined by eq. 15 represents variations of atomic density  $\rho(r)$  with respect to the mean atomic density  $\rho_0$ . In other words the PDF is a measure of the probability of finding an atom at a distance  $r$  from another atom and gives information about both average and the local structure of materials. Quantitative information about the local atomic structure can be extracted from the peaks profiles appearing on  $G(r)$ , for example:

- peak position gives information about atomic bond length,
- peak width represents length distribution of atomic bonds,
- peak area corresponds to the average coordination number.

The total pair distribution function for  $\text{Pd}_{81}\text{Si}_{19}$  alloy is illustrated in Figure 13, in which roman numerals denote respective coordination shells. Mean atomic density  $\rho_0$  was obtained by fitting  $G(r)$  on low  $r$ -range  $\langle 0, 2.0 \rangle \text{ \AA}$  with equation  $-4\pi r\rho_0$  and acquired value is  $0.067 \text{ atoms/\AA}^3$ . Figure 14 shows detailed view of the first coordination shell appearing on  $RDF(r)$  together with interatomic bond lengths  $R_{ij}$  (sum of Goldschmidts radii) and corresponding weight factors  $w_{ij}$  calculated at  $q = 0 \text{ \AA}^{-1}$  using eq. 4.

Three pair distribution functions calculated by various values of  $q_{max}$  in eq. 15 are illustrated in Figure 15, which shows how increasing value of  $q_{max}$  improves resolution

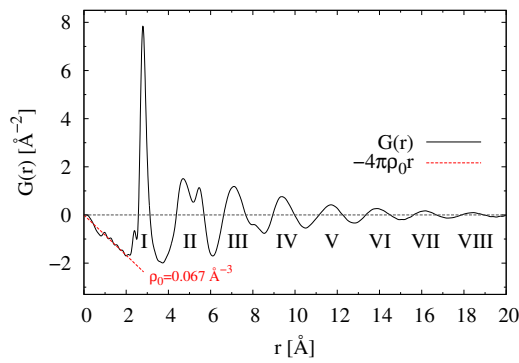


**Figure 13:** Total pair distribution function  $G(r)$  for  $\text{Pd}_{81}\text{Si}_{19}$  alloy. The red dashed line represents fit to  $G(r) = -4\pi r \rho_0$ , from which the average atomic number density  $\rho_0$  was extracted.

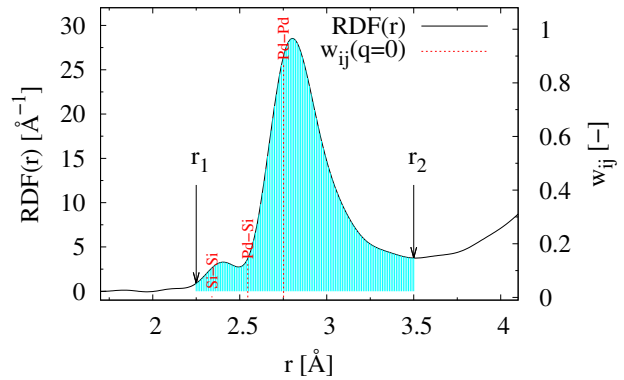


**Figure 14:** The first coordination shell as appearing on  $\text{RDF}(r)$  for  $\text{Pd}_{81}\text{Si}_{19}$  alloy. Vertical lines denote atomic separations for different atomic pairs with corresponding X-ray weights  $w_{ij}$  (calculated for  $q = 0 \text{ \AA}^{-1}$  using eq. 4).

of PDF in real space. As can be seen from Figure 15, the Fourier transform of the first sharp peak of  $S(q)$  is perfectly matching oscillations on  $G(r)$  for distances  $r$  larger than  $9 \text{ \AA}$ . This shows that the first sharp peak of  $S(q)$  is closely related to the medium range order (in the range  $9\text{-}20 \text{ \AA}$ ).

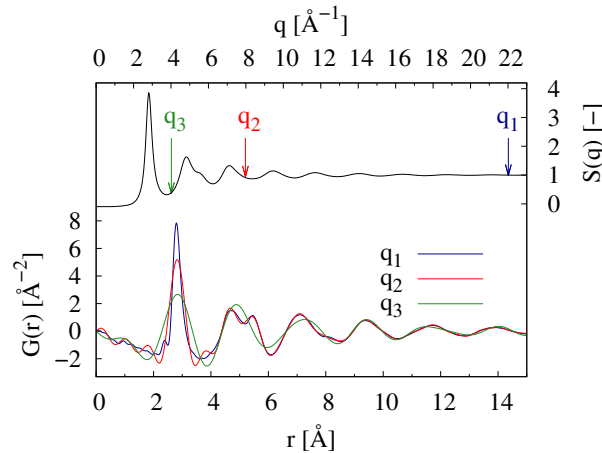


**Figure 15:** Structure factor  $S(q)$  and reduced pair distribution function  $G(r)$  for the  $\text{Pd}_{81}\text{Si}_{19}$  alloy, computed by Fourier transformation on various  $q$ -ranges  $< 0, q_i > \text{\AA}^{-1}, i = 1, 2, 3$  ( $q_1 = 22 \text{ \AA}^{-1}, q_2 = 8 \text{ \AA}^{-1}, q_3 = 4 \text{ \AA}^{-1}$ ).

## 6 In situ X-ray diffraction

This part of the project demonstrates the use of PDF method on real data obtained from the in-situ XRD measurement during constant rate heating. For this reason, amorphous  $\text{Fe}_{76}\text{Mo}_8\text{Cu}_1\text{B}_{15}$  alloy in the form of thin ribbon was used. All XRD experiments were

done at the BW5 beamline of DORIS III accelerator, which operated at fixed photon energy of 100 keV, ( $\lambda = 0.123984 \text{ \AA}$ ). Diffraction patterns were measured in temperature range from  $-194.9^\circ\text{C}$  to  $301.3^\circ\text{C}$  with heating rate  $20^\circ\text{C}/\text{min}$ . Calculated total structure factor,  $S(q)$ , and PDF,  $G(r)$ , for starting temperature ( $-194.9^\circ\text{C}$ ) are shown in Figure 16 and in Figure 17, respectively.

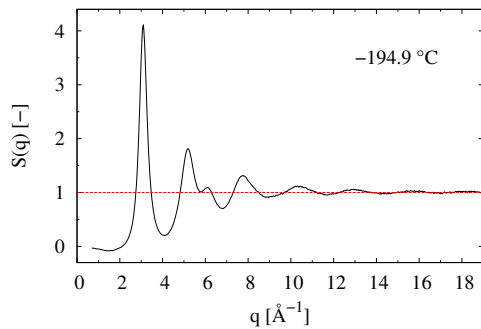


**Figure 16:** X-ray total structure factor  $S(q)$  for  $\text{Fe}_{76}\text{Mo}_8\text{Cu}_1\text{B}_{15}$  alloy.

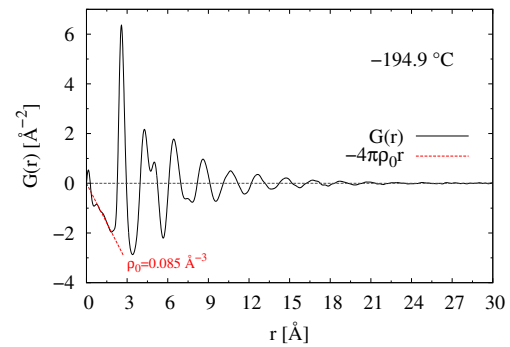


**Figure 17:** Total PDF  $G(r)$  for  $\text{Fe}_{76}\text{Mo}_8\text{Cu}_1\text{B}_{15}$  alloy and extracted value of  $\rho_0$ .

Total structure factors and PDFs for  $\text{Fe}_{76}\text{Mo}_8\text{Cu}_1\text{B}_{15}$  alloy were calculated also for every measured XRD pattern (for every temperature), what is shown in Figures 18 and 19.

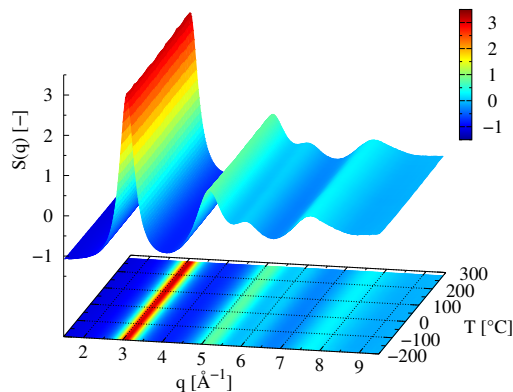


**Figure 18:** Series of calculated structure factors illustrated as a function of temperature  $T$ .

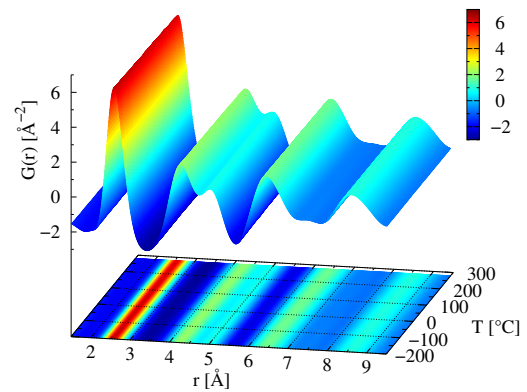


**Figure 19:** Series of calculated PDFs illustrated as a function of temperature  $T$ .

Series of curves presented in Figure 18 show almost no temperature dependence, which is demonstrated by the same qualitative behavior of structure factors in investigated temperature range. However fitting the profile of the first sharp diffraction peak (FSDP) by pseudo-Voigt function reveals tiny changes in its position. Similar conclusions may be drawn from series of  $G(r)$  (see Figure 19) and the first coordination shell. As proposed by Yavari and co-workers [12] the third power of the principal peak position  $q_1$  of the first sharp peak of  $S(q)$  scales with the coefficient of the volume thermal

expansion  $\alpha^q$  of an isotropic amorphous solid as

$$\left[ \frac{q_1(T_0)}{q_1(T)} \right]^3 = \frac{V(T)}{V(T_0)} = 1 + \alpha^q(T - T_0), \quad (19)$$

where  $V(T)/V(T_0)$  is the reduced mean atomic volume at temperature  $T$ , with the reference temperature  $T_0$  (in this study  $-194.9^\circ\text{C}$ ). Figure 20 shows volume thermal expansion curve as determined from the relative change of the position of the FSDP. This expansion curve shows significant change of its slope at the temperature of  $70 \pm 10^\circ\text{C}$ . This temperature perfectly matches the Curie temperature,  $T_C$ , of amorphous  $\text{Fe}_{76}\text{Mo}_8\text{Cu}_1\text{B}_{15}$  alloy. Volume thermal expansion coefficients  $\alpha^q$  for ferromagnetic and paramagnetic states were obtained by fitting expansion curves to the equation 19 on respective temperature ranges.

Similar analysis can be done in real space, where the third power of the position  $r_1$  of the first coordination shell for  $G(r)$  scales with coefficient  $\alpha^I$

$$\left[ \frac{r_1(T)}{r_1(T_0)} \right]^3 = \frac{V(T)}{V(T_0)} = 1 + \alpha^I(T - T_0). \quad (20)$$

The profile of the first coordination shell was modeled by two Gaussians. Relative change of the mass center of the first coordination shell is shown in Figure 21. Volume thermal expansion curve derived from real space data shows an abrupt change of the slope, which can be attributed to the ferromagnetic-to-paramagnetic transition. Due to the large scatter of data, the estimated value of  $T_C$  is  $90 \pm 20^\circ\text{C}$ .

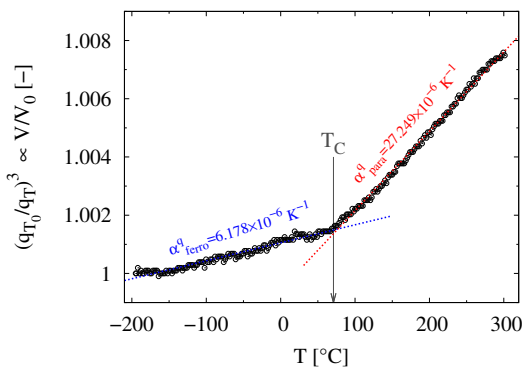


**Figure 20:** Relative change of the center of mass of the first sharp peak of  $S(q)$  during constant rate heating ( $20^\circ\text{C}/\text{min}$ ) (volume thermal expansion curve). Vertical arrow indicate the Curie point  $T_C$ .

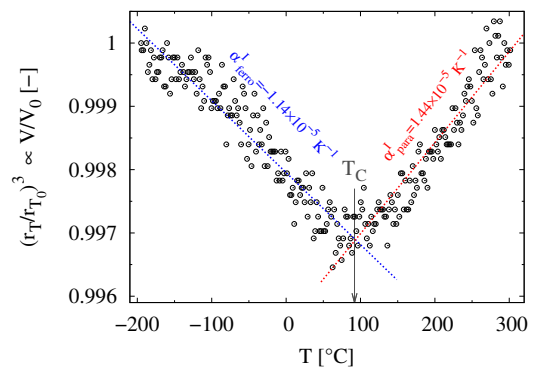


**Figure 21:** Relative change of the center of mass of the first coordination shell during constant rate heating ( $20^\circ\text{C}/\text{min}$ ) (volume thermal expansion curve). Vertical arrow indicate the Curie point  $T_C$ .

In case of real space analysis of data (Figure 21), negative value of the slope of expansion curve is observed under  $T_C$ . The reason why the expansion coefficients for ferromagnetic part of expansion curves have different signs is due to the fact, that both

methods address different length scales. It was shown recently [11], that the FSDP in reciprocal space is related to the medium range order, whereas the first coordination shell on PDF gives information about the nearest atomic neighborhood.

## 7 Conclusions

Methodology of calculation of the atomic pair distribution function from data obtained by two-dimensional detector with all necessary data corrections and steps of calculation were described and explained by using amorphous  $\text{Pd}_{81}\text{Si}_{19}$  alloy. Elaborated methodology was demonstrated on in situ XRD measurements during constant rate heating for amorphous  $\text{Fe}_{76}\text{Mo}_8\text{Cu}_1\text{B}_{15}$  alloy. Temperature behavior of volume change of this sample was investigated by reciprocal space and real space analysis. Moreover, Curie temperature was determined as a change of the slope of expansion curve, what shows that non-magnetic technique such as XRD makes possible to observe ferromagnetic-to-paramagnetic transition of metallic glass. Next advantage of investigating the structure by the pair distribution function is the fact, that unlike other methods it gives information about the nearest atomic neighborhood.

## Acknowledgement

Firstly, I would like to express big thanks to my supervisor Dr. Jozef Bednarčík for his time, for everything, what he taught me and explained to me and for his willing and friendly attitude. Moreover, I thank Mgr. Jana Gamcová and Štefan Michalik for their useful advices and big help during my work. Finally, I thank all organizers of DESY Summer Student Programme 2013, all our lecturers and every participants for this great experience.

## References

- [1] X. Qiu, J. W. Thompson, S. J. L. Billinge, *J. Appl. Cryst.*, **37** (2004) 687
- [2] S. Michalik, *PhD thesis: Utilization of synchrotron radiation for characterization of metallic glasses amorphous structure and their crystallization*, P. J. Safarik University, Kosice, Slovakia, 2011.
- [3] C. Janot *Quasicrystals*, Clarendon printer, 2nd edition, 1995.
- [4] I. Jeong, J. Thompson, T. Proffen, S. Billinge, *PDFgetX: User's Manual*, Michigan State University, East Lansing, MI, USA, 2003.
- [5] T. E. Faber, J. M. Ziman, *Philos. Mag.*, **11**(1965) 153.
- [6] J. A. Nielsen, D. McMorrow, *Elements of modern X-ray physics*, Markono Print Media Pte Ltd, Singapore, 2nd edition, 2011.
- [7] Y. Waseda, *The Structure of Non-Crystalline Materials*, Mc Graw-Hill Inc., the United States of America, 1980.
- [8] B. J. Thijsee, *J. Appl. Cryst.*, **17** (1984) 61.

- [9] D. Waasmaier, A. Kirfel, *Acta Cryst. A* **51** (1995) 416-413.
- [10] T. Egami T., S. J. L. Billinge, *Underneath the Bragg Peaks: Structural analysis of complex materials*, Pergamon Press, Elsevier, Oxford, England, 2003.
- [11] J. Bednarcik, S. Michalik, V. Kolesar, U. Rütt, H. Franz, *Phys. Chem. Chem. Phys.*, **15**(2013) 8470.
- [12] A. Yavari, A. Moulec, A. Inoue, N. Nishiyama, N. Lupu, E. Matsubara, W. Botta, G. Vaughan, M. Michiel and A. Kvik, *Acta Matter*: **53** (2005) 1611.